Transp Porous Med (2005) 58:315–338
DOI 10.1007/s11242-004-1410-x

1-D Modeling of Hydrate Depressurization in Porous Media

X. SUN, N. NANCHARY and K. K. MOHANTY
Department of Chemical Engineering, University of Houston, Houston, TX 77204-4004, USA

(Received: 1 July 2003; accepted in final form: 2 May 2004))

Abstract. A thermal, three-phase, one-dimensional numerical model is developed to simulate two regimes of gas production from sediments containing methane hydrates by depressurization: the dissociation-controlled regime and the flow-controlled regime. A parameter namely dissociation-flow time-scale ratio, R_τ, is defined and employed to identify the two regimes. The numerical model uses a finite-difference scheme; it is implicit in water and gas saturations, pressure and temperature, and explicit in hydrate saturation. The model shows that laboratory-scale experiments are often dissociation-controlled, but the field-scale processes are typically flow-controlled. Gas production from a linear reservoir is more sensitive to the heat transfer coefficient with the surrounding than the longitudinal heat conduction coefficient, in 1-D simulations. Gas production is not very sensitive to the well temperature boundary condition. This model can be used to fit laboratory-scale experimental data, but the dissociation rate constant, the multiphase flow parameters and the heat transfer parameters are uncertain and should be measured experimentally.

Key words: hydrate reservoir, depressurization, modeling, heat transfer, methane hydrates, gas production.

1. Introduction

By all counts, the world-wide energy demand is expected to go up significantly (about 65–172% assuming a net growth rate of 1 or 2% per year, respectively, over the current demand of about 200 barrel of oil equivalent per day) in the next 50 years (Skov, 2003). Renewable and nuclear energy sources supply less than 15% of the total energy consumption today (Moniz and Kenderdine, 2002). Their role is not expected to increase much in the next 20–50 years, barring some drastic technological innovation in these fields. This increase in demand is expected to be met by fossil fuel (oil, gas and coal). Gas hydrates may be one of the fossil fuel resources that is yet untapped, but may play a major role.

Gas hydrates are crystalline, ice-like compounds of gas and water molecules that are formed under certain thermodynamic conditions (Sloan, 1998). They are formed as a result of inclusion of small molecules (namely guest molecules, e.g., methane, ethane, CO_2) inside the cavities of ice-like structures

made by the water molecules. The hydrate formation can be represented by the reaction

$$M(g) + N_H H_2O(l) \Leftrightarrow M \cdot N_H H_2O(s), \tag{1.1}$$

where M is the guest molecule in hydrate formation and N_H (commonly known as hydrate number) is the number of water molecules required per gas molecule to form a gas hydrate. The hydrate number for methane is approximately 6 (Sloan, 1998). The methane concentration in hydrates is much higher than the solubility of methane in liquid water. In fact, the amount of methane in a unit volume of hydrate (at stable pressure and temperature) is approximately 170 times the amount in the same volume at standard conditions.

Hydrate deposits occur naturally within ocean sediments just below the sea floor at temperatures and pressures existing below about 500 m water depth. Gas hydrate also is stable in conjunction with permafrost in the Arctic. Most marine gas hydrate is formed of microbially generated gas. It binds huge amounts of methane into the sediments. Worldwide, gas hydrate is estimated to hold about 10^{16} kg of organic carbon in the form of methane (Kvenvolden *et al.*, 1993). This represents an amount of organic carbon that is twice as much as in all other fossil fuels on earth (conventional natural gas, oil, and coal) and an amount of methane that is about 3,000 times as much as what exists in the atmosphere. Gas hydrate is important primarily because it contains huge amounts of methane in a concentrated form and because it influences the physical properties of sedimentary deposits, particularly sediment strength.

Finding an efficient, safe method of producing natural gas from hydrate deposits is important commercially. The three methods being explored for hydrate production are: (1) depressurization, in which pressure is lowered inside the well encouraging the methane hydrate to dissociate; (2) thermal stimulation, in which the reservoir is heated above the dissociation temperature using hot water or steam, and (3) inhibitor injection, in which methanol or brine is used to disequilibrate the hydrate. Combinations of these methods can also be used for enhanced recovery of natural gas.

Several models were proposed for gas production from hydrates in the past few years (Tsypkin, 1991; Ji *et al.*, 2001; Moridis, 2002). In most analytical models, the mobility of the water phase is ignored (Ji *et al.*, 2001). The analytical model by Tsypkin (1991) takes into account the flow of water, but it assumes a fixed relative permeability for each phase. Most of the analytical models assume equilibrium decomposition (Tsypkin, 1991; Ji *et al.*, 2001). In these models, hydrate is assumed to dissociate instantaneously once the equilibrium condition is reached. Experimental work by Makogon and Holditch (2001) and Stern *et al.* (1996) suggests otherwise. Kinetic models of pure hydrate dissociation have been proposed by Kim *et al.* (1987) and

Clarke and Bishnoi (2000, 2001). Yousif *et al.* (1991) have considered kinetics and multiphase flow for the depressurization process, but under isothermal conditions. Moridis (2002) has developed a module called EOSHYDR2 for a general-purpose simulator TOUGH2 that can model hydrate depressurization.

The goal of this work is to develop a 1-D simulator for quick interpretation of laboratory experiments, and identification of important parameters for field-scale production. We consider the laboratory case in which the hydrate-bearing medium has a size typical of the core samples used in laboratory studies and the field case where methane gas is produced from a small hydrate reservoir. The numerical simulator includes dissociation thermodynamics, kinetics, multiphase flow and heat transfer for hydrate depressurization above the quadruple point. The energy balance equation incorporates heat conduction, convection and transfer from the surroundings. The simulator is fast and self-standing. The Section 2 describes the mathematical model for hydrate depressurization. The numerical model is described in Section 3. The results are discussed in Section 4, followed by key conclusions in the last section.

2. Hydrate Depressurization Model

Let us assume that the dissociation occurs in a hydrate-bearing medium of length L. The medium is supposed to be saturated with a mixture of water (or gas) and methane hydrate in equilibrium under hydrate stable conditions of pressure p^0 and temperature T^0. Let t denote the time and x the spatial location. At time $t = 0$, a pressure p_0 below the equilibrium pressure p_e is imposed on the medium at $x = 0$ (for convenience, we call this location ''production well'' from now on), and is maintained constant thereafter. The hydrate near the production well becomes unstable and dissociates to give natural gas and water. Due to the ''communication'' of pressure and thermal state between inside and outside of the medium, the dissociation process continues to expand inside the medium. The porous medium skeleton is assumed to be non-deformed; the gas hydrate is supposed to be structure I methane hydrate; methane can occur only in gaseous and hydrate states; water can occur only in liquid and hydrate states, i.e., ice and water vapor formation are neglected. The temperature is assumed to stay above the hydrate–gas–water–ice quadruple point.

The mass balance equations for gas and water flow through the porous medium can be written as

$$\frac{\partial}{\partial t}(\phi \rho_g S_g) + \frac{\partial}{\partial x}(\rho_g v_g) = \dot{m}_g, \tag{2.1}$$

$$\frac{\partial}{\partial t}(\phi\rho_{\mathrm{w}}S_{\mathrm{w}}) + \frac{\partial}{\partial x}(\rho_{\mathrm{w}}v_{\mathrm{w}}) = \dot{m}_{\mathrm{w}}, \tag{2.2}$$

where ϕ is the porosity of the hydrate bearing medium, S is the saturation, which is defined as the fraction of the total (fluid + hydrate) pore volume, ρ is the density, v is the Darcy velocity, $\dot{m}$ represents the local mass rate produced by hydrate decomposition per unit volume. The subscripts 'g' and 'w' refer to gas phase (methane) and liquid phase (water), respectively. In this paper, the water phase is assumed to be incompressible. The methane is assumed to follow the van der Waals equation of state.

The conservation equation of the solid hydrate is given as:

$$\frac{\mathrm{d}}{\mathrm{d}t}(\phi\rho_{\mathrm{h}}S_{\mathrm{h}}) = -\dot{m}_{\mathrm{h}}, \tag{2.3}$$

where the subscript 'h' refers to the hydrate phase. $\dot{m}_{\mathrm{h}}$ represents the local mass rate of hydrate dissociated per unit volume. The generation rates of gas and water are related by stoichiometry of the hydrate and related to dissociation rate of the hydrate by the following:

$$\dot{m}_{\mathrm{h}} = \dot{m}_{\mathrm{g}}\frac{N_{\mathrm{H}}M_{\mathrm{w}} + M_{\mathrm{g}}}{M_{\mathrm{g}}}, \tag{2.4}$$

$$\dot{m}_{\mathrm{w}} = \dot{m}_{\mathrm{g}}\frac{N_{\mathrm{H}}M_{\mathrm{w}}}{M_{\mathrm{g}}}, \tag{2.5}$$

here M_{w} and M_{g} are the molecular weight of water and gas (in this paper, methane), respectively.

The rate of gas generation caused by hydrate dissociation is given by the Kim–Bishnoi model (Kim *et al.*, 1987):

$$\dot{m}_{\mathrm{g}} = k_{\mathrm{d}}A_{\mathrm{s}}(f_{\mathrm{e}} - f), \tag{2.6}$$

k_{d} is the dissociation constant ($\mathrm{kg/m^2\,Pa\,s}$), f is the local gas fugacity and f_{e} is the gas fugacity in equilibrium with water and gas hydrate. In this work, we used local gas pressure p and methane-water-hydrate equilibrium pressure p_{e} to approximate f and f_{e}, respectively, as in the work by Yousif *et al.* (1991). Thermodynamic equilibrium relationship between p_{e} and temperature, T, is given by Sloan (1998). It can be affected by salinity and porous medium structure itself (Wilder and Smith, 2002). In this work, the hydrate equilibrium pressure, p_{e}, is evaluated by

$$p_{\mathrm{e}} = 1.15\,\exp\left(49.3185 - \frac{9459}{T}\right). \tag{2.7}$$

This equation describes the equilibrium pressure of hydrate, gas and water phase above quadruple point. p_{e} is in Pa and T is in Kelvin.

A_s in Equation (2.6) is the interface area between hydrate and fluid phases, which is estimated with the method by Amyx *et al.* (1960) in this paper:

$$A_s = \left(\frac{\phi_{wg}^3}{2K}\right)^{0.5}, \tag{2.8}$$

where K is the absolute permeability (m^2) and ϕ_{wg} is the porosity occupied by gas and water. This model assumes hydrates to be coating the sand grains uniformly; this assumption has not been validated. ϕ_{wg} is given by:

$$\phi_{wg} = (1 - S_h)\phi. \tag{2.9}$$

As the depressurization proceeds, the pore volume occupied by gas and water and thus permeability increases with time. An empirical relationship (Amyx *et al.*, 1960; Yousif *et al.*, 1991) between ϕ_{wg} and K for Berea sandstone is given by

$$K = \begin{cases} 5.51721(\phi_{wg})^{0.86}, & \phi_{wg} < 0.11, \\ 4.84653 \times 10^8(\phi_{wg})^{9.13}, & \phi_{wg} \geqslant 0.11. \end{cases} \tag{2.10}$$

The unit of the permeability given by Equation (2.10) is md ($\sim 10^{-15}\ m^2$). There have been few measurements of petrophysical properties of porous media with hydrates; many of the empirical models assumed here are extensions of relations used in the literature for non-hydrate systems.

The velocities of gas and water in Equations (2.1) and (2.2) are given by the Darcy's law for multiphase flow, i.e.,

$$v_g = -\frac{K(S_h)k_{rg}(S_w, S_g)}{\mu_g}\frac{\partial p_g}{\partial x}, \tag{2.11}$$

$$v_w = -\frac{K(S_h)k_{rw}(S_w, S_g)}{\mu_w}\frac{\partial p_w}{\partial x}. \tag{2.12}$$

In this paper the relative permeability functions k_{rg} (S_w, S_g) and k_{rw} (S_w, S_g) are evaluated with Corey model:

$$k_{rw} = \left(\frac{\frac{S_w}{S_w + S_g} - S_{wr}}{1 - S_{wr} - S_{gr}}\right)^{n_w}, \tag{2.13}$$

$$k_{rg} = \left(\frac{\left(\frac{S_g}{S_w + S_g}\right) - S_{gr}}{1 - S_{wr} - S_{gr}}\right)^{n_g}. \tag{2.14}$$

In Equation (2.13), the residual water saturation and gas saturation, S_{wr} and S_{gr}, are based on the pore volume occupied by fluid phases (namely effective pore volume). Note that, S_w and S_g, are based on the total pore volume (occupied by fluid phases and hydrates) and the ratio $S_g/(S_w + S_g)$

(or $S_w/(S_w + S_g)$) denotes the effective pore volume-based saturation. In this paper, we assumed a value of 0.2 for S_{wr} and 0 for S_{gr}, respectively. Corey models are commonly used models, but are not applicable to all porous media. They should be used only if they match experimental measurements for any specific medium.

The water viscosity, μ_w(cp), is assumed to be constant. The gas (methane) viscosity, μ_g(cp), as a function of temperature and density is given by (Selim and Sloan, 1989):

$$\begin{aligned}\mu_g = {} & 2.4504 \times 10^{-3} + 2.8764 \times 10^{-5} T + 3.279 \times 10^{-9} T^2 \\ & - 3.7838 \times 10^{-12} T^3 + 2.0891 \times 10^{-5} \rho_g + 2.5127 \times 10^{-7} \rho_g^2 \\ & - 5.822 \times 10^{-10} \rho_g^3 + 1.8378 \times 10^{-13} \rho_g^4, \end{aligned} \tag{2.15}$$

where temperature T is in Kelvin and the density is in kg/m^3.

The pressure of gas phase and water differs by the capillary pressure, p_c, i.e.,

$$p_c = p_g - p_w. \tag{2.16}$$

In this paper, p_c takes the functional form:

$$\frac{p_c}{p_c^e} = h_c(S_w) = \left(\frac{\frac{S_w}{S_w + S_g} - S_{wr}}{1 - S_{wr}} \right)^{-n_c}, \tag{2.17}$$

Here p_c^e is the entry pressure and h_c is the normalized capillary pressure.

The saturations satisfy the following equation:

$$S_g + S_w + S_h = 1. \tag{2.18}$$

Substituting the generalized Darcy's law for water and gas into mass balance equations (2. 1) and (2. 2), we get:

$$\frac{\partial}{\partial t}(\phi \rho_g S_g) - \frac{\partial}{\partial x}\left(\rho_g \frac{K k_{rg}}{\mu_g} \frac{\partial p_g}{\partial x} \right) = \dot{m}_g, \tag{2.19}$$

$$\frac{\partial}{\partial t}(\phi \rho_w (1 - S_g - S_h)) - \frac{\partial}{\partial x}\left(\rho_w \frac{K k_{rw}}{\mu_w} \left(\frac{\partial p_g}{\partial x} - \frac{\partial p_c}{\partial x} \right) \right) = \dot{m}_w. \tag{2.20}$$

Hydrate dissociation is an endothermic process and the dissociation rate depends strongly upon the temperature. In the model by Ji *et al.* (2001), the heat transfer between the hydrate zone and the surrounding sediments was neglected. Only convection within the gas phase, Joule–Thompson throttling effect, and adiabatic effect were accounted for. In this paper, we adopt a 1D continuum heat transfer model with conduction, convection and heat flow from the surrounding sediments. This model is based on the assumption of no inter-phase heat resistance between gas, water, hydrate and the sand

forming the medium. The thermal energy balance equations can be written in terms of enthalpy and temperature:

$$\frac{\partial}{\partial t}[\phi(\rho_g S_g H_g + \rho_w S_w H_w + \rho_h S_h H_h) + (1-\phi)\rho_s H_s] + \frac{\partial}{\partial x}(\rho_g v_g H_g + \rho_w v_w H_w) = \frac{\partial}{\partial x}\left(\lambda \frac{\partial T}{\partial x}\right) + q, \tag{2.21}$$

where H_i is the enthalpy for phase i and the subscript 's' means the sand phase, T is the local temperature, and λ is the heat conductivity of hydrate-bearing medium, which is a function of local composition of the medium. The heat transfer, q from the surroundings can be written as:

$$q = \frac{P}{A_c}\alpha(T_s - T), \tag{2.22}$$

here P/A_c is the ratio of the perimeter to the area of the cross section of the medium, α is the heat transfer coefficient and T_s is the surrounding temperature.

Inserting mass balance equations (Equations (2.1)–(2.3)) and the definition of latent heat of hydrate dissociation: $\dot{m}_g H_g + \dot{m}_w H_w - \dot{m}_h H_h = \dot{m}_h \Delta H_D$ into Equation (2.21), we get:

$$(1-\phi)\frac{\partial}{\partial t}(\rho_s H_s) + \phi\left(\rho_g S_g \frac{\partial H_g}{\partial t} + \rho_w S_w \frac{\partial H_w}{\partial t} + \rho_h S_h \frac{\partial H_h}{\partial t}\right) + \rho_g v_g \frac{\partial H_g}{\partial x} + \rho_w v_w \frac{\partial H_w}{\partial x} = \frac{\partial}{\partial x}\left(\lambda \frac{\partial T}{\partial x}\right) + q - \dot{m}_h \Delta H_D, \tag{2.23}$$

where ΔH_D is the enthalpy change in hydrate decomposition. The process of hydrate decomposition is an endothermic phase change process. The latent heat of hydrate dissociation above quadruple point is given as (Selim and Sloan, 1989):

$$\Delta H_D = 446.12 \times 10^3 - 132.638 T \,\mathrm{J/kg}, \quad 273\mathrm{k} < T < 298\,\mathrm{K}. \tag{2.24}$$

Note that

$$\mathrm{d}H_i = \frac{\partial H_i}{\partial T}\mathrm{d}T + \frac{\partial H_i}{\partial p_i}\mathrm{d}p_i = C_{pi}\mathrm{d}T + \sigma_i \mathrm{d}p_i,$$

where the subscript i refers to gas, water, or hydrate. Here, C_{pi} is the heat capacity and σ_i is the throttling coefficient for the ith phase, respectively. For the sand phase,

$$\mathrm{d}H_s = \frac{\partial H_s}{\partial T}\mathrm{d}T = C_{ps}\,\mathrm{d}T.$$

We neglect the effect of pressure on enthalpy for water and hydrate phases. We also assume a single-temperature model, i.e., neglect any heat transfer

barrier between phases inside a grid block (Nozad *et al.*, 1985). We use Equation (2.22) for heat transfer from surroundings, q. Thus, Equation (2.23) becomes:

$$\begin{aligned}&(\phi(\rho_g S_g C_{pg} + \phi\rho_w S_w C_{pw} + \phi\rho_h S_h C_{ph} + (1-\phi)\rho_s C_{ps})\frac{\partial T}{\partial t}\\&\quad + (\rho_g v_g C_{pg} + \rho_w v_w C_{pw})\frac{\partial T}{\partial x} - \frac{\partial}{\partial x}\left(\lambda\frac{\partial T}{\partial x}\right)\\&\quad = -\dot{m}_h \Delta H_D - \phi\rho_g S_g \sigma_g \frac{\partial p_g}{\partial t} - \rho_g v_g \sigma_g \frac{\partial p_g}{\partial x} + \frac{P}{A_c}\alpha(T_s - T).\end{aligned} \tag{2.25}$$

The following specific heat data are used (Selim and Sloan, 1989):

$$C_{pw} = 4023.976 + 0.57736T - 8.314\times10^{-5}T^2\ \mathrm{J/kg\,K}, \tag{2.26}$$

$$C_{pg} = 1238.79 + 3.1303T + 7.905\times10^{-4}T^2 - 6.858\times10^{-7}T^3\ \mathrm{J/kgK}, \tag{2.27}$$

$$C_{ph} = 2220\ \mathrm{J/kg\,K}, \tag{2.28}$$

$$C_{ps} = 835\ \mathrm{J/kg\,K}. \tag{2.29}$$

Van der Waals equation was used to calculate throttling effect caused by the expansion of the gas phase, and the data in Tester (1997) can be used to calculate the throttling effect. The throttling coefficient for methane is given by:

$$\sigma_g \equiv \left(\frac{\partial H_g}{\partial P_g}\right)_T \approx -1.5\times10^{-4}\ \mathrm{J/kg\,Pa}. \tag{2.30}$$

The heat conduction coefficient, λ, is a function of the local composition of the hydrate-bearing medium.

Initial conditions are as follows:

$$\begin{aligned}&S_g = S_g^0, \quad S_w = S_w^0, \quad S_h = S_h^0 \quad \text{at } t = 0,\\&p_g = p_g^0 \quad \text{at } t = 0,\\&T = T^0 \quad \text{at } t = 0.\end{aligned} \tag{2.31}$$

The following boundary conditions are imposed:

$$\begin{aligned}&p_g = p_0, \quad p_c = p_c^e \quad \text{at } x = 0,\\&\tfrac{\partial p_g}{\partial x} = 0, \quad \tfrac{\partial p_w}{\partial x} = 0 \quad \text{at } x = L,\\&T = T_0 \quad \text{at } x = 0,\\&\tfrac{\partial T}{\partial x} = 0 \quad \text{at } x = L.\end{aligned} \tag{2.32}$$

This temperature boundary condition at the well applies in the case when the temperature in production well is fixed (base case). Another temperature boundary condition:

$$\frac{\partial T}{\partial x} = 0 \quad \text{at } x = 0, \tag{2.33}$$

that corresponds to an insulated well is also used to study the influence of well boundary condition on gas production performance.

3. Numerical Formulation

Self-similar solutions to the above problem can only be obtained under unrealistic simplifications (Tsypkin, 1991; Ji *et al.*, 2001). Numerical solution is sought in this work. The equations governing the water and gas flow and hydrate decomposition can be reduced to their dimensionless form as follows:

$$\frac{\partial(r_g S_g)}{\partial \tau_f} - \frac{\partial}{\partial x_D}\left(\frac{K k_{rg} r_g}{K_{max} r_v}\frac{\partial p^*}{\partial x_D}\right) = \frac{L \dot{m}_g}{V_{char}\rho_{g0}}, \tag{3.1}$$

$$\frac{\partial S_w}{\partial \tau_f} - R_M \frac{\partial}{\partial x_D}\left(\frac{K k_{rw}}{K_{max}}\frac{\partial p^*}{\partial x_D} - \frac{1}{N_{ca}}\frac{K k_{rw}}{K_{max}}\frac{dh_c}{dS_w}\frac{\partial S_w}{\partial x_D}\right) = \frac{L \dot{m}_w}{V_{char}\rho_w}, \tag{3.2}$$

$$\frac{dS_h^*}{d\tau_D} = -\frac{\dot{m}_h}{\dot{m}_{h,max}}. \tag{3.3}$$

In the above equations:

$$x_D = x/L, \tag{3.4}$$

$$\tau_f = \frac{V_{char} t}{\phi L}, \tag{3.5}$$

$$\tau_D = \frac{\dot{m}_{h,max} t}{S_{h,max}\phi\rho_h}, \tag{3.6}$$

$$p^* = \frac{p_g - p_0}{p^0 - p_0}, \tag{3.7}$$

$$r_g = \frac{\rho_g}{\rho_{g0}}, \tag{3.8}$$

$$r_v = \frac{\mu_g}{\mu_{g0}}, \tag{3.9}$$

$$R_M = \frac{\mu_{g0}}{\mu_w}, \tag{3.10}$$

$$N_{ca} = \frac{p_g^0 - p_0}{p_c^e}, \tag{3.11}$$

$$K_{max} = K(\phi), \tag{3.12}$$

$$V_{\text{char}} = \frac{K_{\max}}{\mu_{g0}} \frac{p_g^0 - p_0}{L}, \tag{3.13}$$

$$\dot{m}_{h,\max} = k_d(T^0) A_{s,\max}(p_e - p_0), \tag{3.14}$$

$$S_h^* = \frac{S_h}{S_{h,\max}} = \frac{S_h}{S_h^0}, \tag{3.15}$$

ρ_{g0} and μ_{g0} are the density and the viscosity of the gas phase at initial reservoir conditions, respectively. The maximum dissociation surface area, $A_{s,\max}$, can be obtained by analyzing Equation (2.8), which gives a maximum value at $\phi_{wg} = 0.11$.

The characteristic velocity of the flow, V_{char}, is defined as the gas velocity corresponding to the maximum permeability, which is evaluated with the total porosity (the pore space occupied by fluid phases and the hydrate phase), and the largest driving force (Equation (3.13)). Actually, under most cases, the flow rate cannot reach the characteristic velocity, because the chance that the effective permeability and the pressure drop simultaneously reach the maximum value is very low.

In this paper, the governing equations are solved in a sequential manner: the dissociation equation (3.3) is solved explicitly first; the mass balance equations (3.1) and (3.2) are simultaneously solved next, followed by implicit solution of the heat transfer equation (2.25). Upstream evaluation of phase mobility is employed in spatial discretization of the equations.

One issue that is associated with the sequential solution of the governing equations is the determination of the simulation time step. If the time step is not chosen correctly, instability (caused by the explicit scheme in solving the dissociation equation) may arise and even wrong solution may be obtained from the simulation. In this work, the time step is chosen according to Courant–Friedrichs–Lewy CFL stability criterion, i.e., in each simulation step, CFL criterion was applied to each governing equation to determine the largest time step that can ensure the stability of that equation, and the smallest of those time steps (for all equations) was taken as the actual simulation time step.

The whole dissociation process can be physically viewed as four threads evolving in parallel: the decomposition of gas hydrate, the heat transfer, the flow of the water and the flow of the gas through the medium, The time scale characterizing these four threads may differ by several orders of magnitude, but the simulator should evolve the processes with the same physical time step. Thus, the simulation time step is taken according to the CFL stability criterion of the thread that evolves most rapidly.

A parameter, namely dissociation-flow time-scale ratio, can be proposed to reflect the relative importance of the fluid flow and the hydrate decomposition. The dissociation–flow time-scale ratio is defined as:

$$R_\tau = \frac{\tau_f}{\tau_D} = \frac{V_{char} S_{h,max} \rho_h}{L \dot{m}_{h,max}}. \tag{3.16}$$

The physical meaning of R_τ can be clarified from the definition of τ_f and τ_D (Equations (3.5) and (3.6)). τ_f means the amount of gas in number of pore volumes flowing out of the medium at the characteristic (maximum) flow rate in physical time t. τ_D is the fraction of hydrate dissociated in physical time t, or it can be seen as the gas produced by decomposition of hydrate in physical time t as a fraction of total gas stored in hydrate. Thus R_τ is a qualitative indication of the relative importance of the flow mechanism and dissociation mechanism. At large values of R_τ, flow is a faster process and the system is increasingly controlled by dissociation; otherwise, the system is controlled by flow.

4. Results

Numerical results of two base cases are shown, one in a laboratory-scale and the other under typical field conditions. For the base cases, mechanisms that control the hydrate dissociation processes are identified with the dissociation–flow time-scale ratio. The results for both cases were modeled with 50 spatial grid blocks. All the simulations were performed on a Pentium IV 2.2 GHz PC. Comparison of the simulation results of different number of grid blocks (shown later) indicates that simulation of 50 grid blocks gives satisfactorily accurate results for the cases used in this paper. A set of experimental data is then matched by tuning the parameters of the laboratory-scale simulation. Finally, the field-scale numerical results are compared with the analytical solution obtained by Ji *et al.* (2001).

The properties characterizing the laboratory-scale and the field-scale systems used in base case simulations are listed in Table I. The field-scale simulation takes a small hydrate reservoir with 100 m in length, and the laboratory-scale uses a core sample of 15 cm.

Table II lists the time-scale ratio and controlling mechanism of each case. Clearly, the time-scale ratio of laboratory-scale case (5.24E+3) is significantly higher than that of the field-scale case (1.76E−4). This indicates that the fluid flow is relatively faster in the laboratory-scale case and the gas production is controlled by the hydrate decomposition; on the other hand, the field-scale simulation is flow-controlled.

Figure 1 shows pressure, saturation and temperature distributions for thermal simulation with BC1 (fixed temperature in production well) of the base case in the laboratory-scale. In laboratory-scale, the whole process can be divided into two stages. In the first stage, because of the fast fluid flow rate after the beginning of the depressurization, the pressure inside the medium

Table I. Parameters for the base cases

ϕ (%)	18.8	P_0 (Mpa)	2
ρ_h (g/cm^3)	0.91	T_0 (K)	287
ρ_w (g/cm^3)	1	T_s (K)	287
ρ_s (g/cm^3)	2.67508	k_d (kg/m^{2}Pa s)	4.4E−16
μ_w (cp)	1	n_w (Equation (2.13))	4.0
S_w^0 (%)	30	n_g (Equation (2.14))	2.0
S_h^0 (%)	69	p_c^e (MPa) (Equation(2.17))	4.0E−3
S_g^0 (%)	1	n_c (Equation (2.17))	0.65
p^0 (MPa)	15	λ (W/m K)	5.57 (dissociated zone) 2.73 (hydrate zone)
T^0 (K)	287	α (W/m^2 K)	5.2

Table II. Time-scale ratio and controlling mechanism of each case

	Laboratory-scale	Field-scale
R_τ	5.24E+3	1.76E−4
Controlling process	Dissociation	Flow

drops below equilibrium pressure in a very short time (within 0.24 min, as shown in Figure 1). In this stage, the amount of dissociated hydrate can almost be neglected, as indicated by Figure 1(b), which shows little change of hydrate saturation during this period. It can also be observed from Figure 1(c) that the temperature almost keeps at the initial value through this stage. In the second stage, the hydrate dissociates under a nearly uniform pressure distribution within the medium, and the hydrate saturation decreases almost uniformly, implying a nearly uniform dissociation rate along the core. At the same time, the temperature decreases nearly uniformly.

Figure 2(a)–(c) shows pressure, saturation and temperature distributions for thermal simulation with BC1 (fixed temperature in production well) of the field-scale base case. As can be seen from Figure 2, the whole reservoir can be divided into three distinct zones: the dissociated zone, the dissociation zone and the ''untouched'' zone. The dissociated zone is immediately adjacent to the production well, and the hydrate saturation is depleted in this region. The ''untouched'' zone lies adjacent to the no-flow boundary. In this region, the pressure is above the equilibrium dissociation pressure, thus no dissociation takes place in this region and the hydrate saturation is at its initial value. Hydrate decomposition occurs only in a narrow region in the field-scale reservoir. This region, namely the dissociation zone, lies between the dissociated region and the ''untouched'' region. The pressure in this region is below the equilibrium pressure and the hydrate saturation is not completely

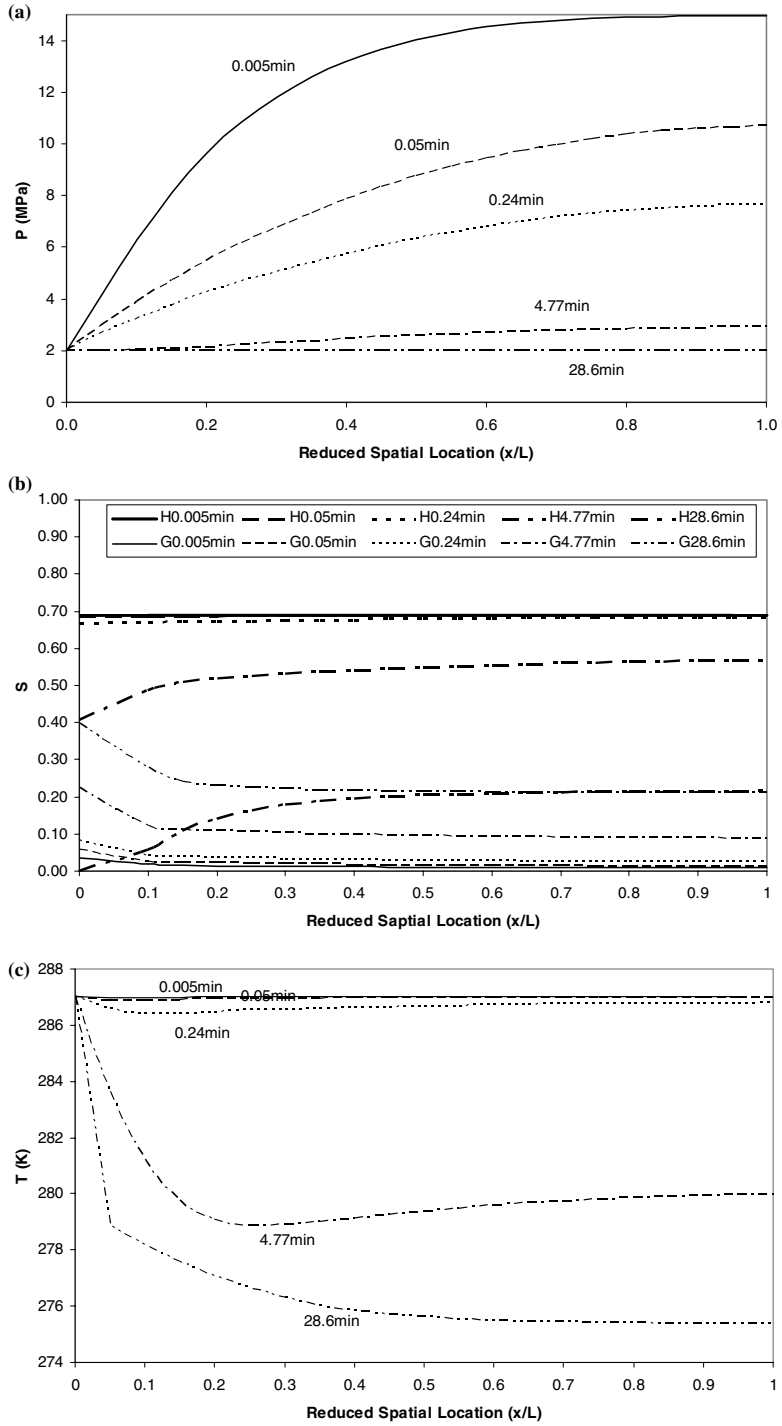

Figure 1. (a) Laboratory-scale pressure profile. (b) Laboratory-scale saturation profile (H: hydrate, G: gas). (c) Laboratory-scale temperature profile.

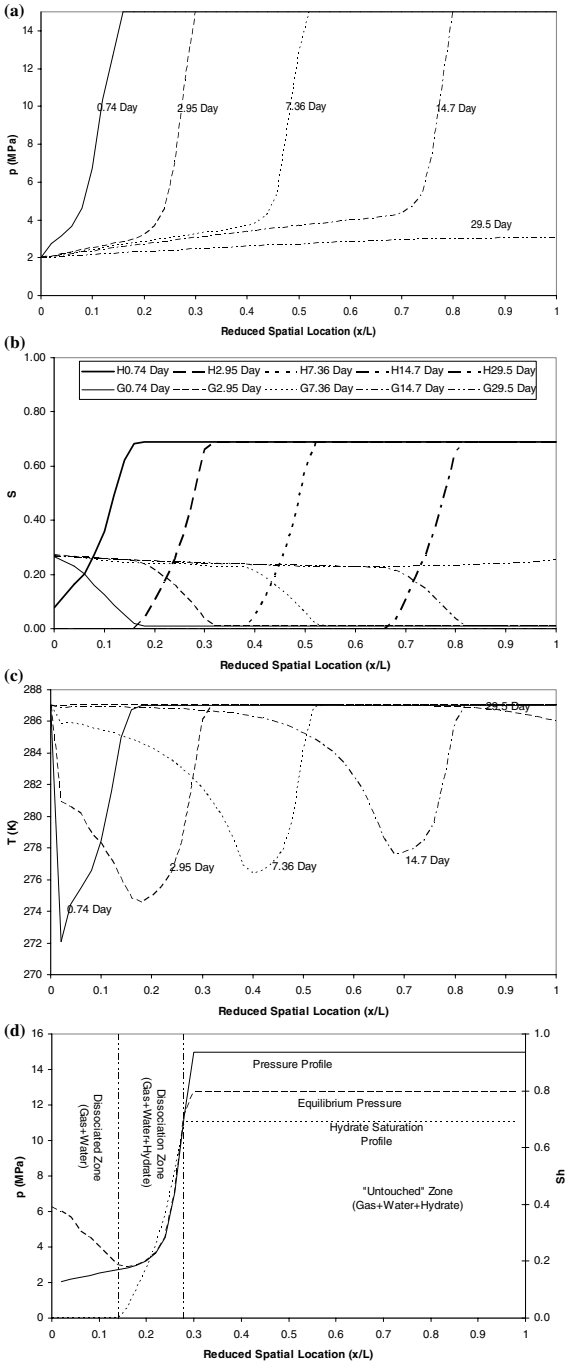

Figure 2. (a) Field-scale pressure profile. (b) Field-scale saturation profile (H: hydrate, G: gas). (c) Field-scale temperature profile. (d) Three zones in reservoir: dissociated zone, zone under dissociation and zone waiting for dissociation.

depleted. Figure 2(d) shows the typical pressure distribution, equilibrium pressure at the reservoir temperature, and hydrate saturation in the three zones in the reservoir at 2.95 days after the start of depressurization. Although the dissociation zone is fairly narrow in comparison with the other two zones, it is a 'zone' instead of an 'interface'. A self-similar solution was obtained elsewhere (Ji *et al.*, 2001) assuming equilibrium decomposition, which gave rise to a dissociation interface. Clearly, kinetic barriers give a much different solution (Figure 2(d)). Another self-similar solution (Tsypkin, 1991) was obtained for a mathematical model with the assumption of an extended dissociation zone instead of a dissociation interface, but equilibrium dissociation was still assumed. From Figure 2(d), one can see that, in a significant part of the dissociating zone, the local pressure is lower than the equilibrium pressure.

The pressure, saturation and temperature profiles in the field case have a steep front located at the hydrate decomposition region (Figure 2(a)–(c)), while the profiles in the laboratory case do not have a steep front (Figure 1(a)–(c)). The relatively lower pressure gradient in the field-scale reservoir generates a relatively lower fluid flow rate in comparison with the laboratory-scale core. As shown, in Table II, R_τ is much higher for the laboratory case than for the field case and thus field case is flow-controlled.

Figure 3 shows the pressure profiles for the field case obtained from simulations with 20, 50 and 200 grid blocks. The pressure profiles of 50 grid blocks are close to the profiles of 200 grid blocks, indicating that 50 grid blocks can give sufficiently accurate results for the cases studied in this paper. Temperature saturation profiles and the gas production (not shown as figures here) show the same trend with grid refinement.

Figures 4 and 5 show the sensitivity of the results to the temperature boundary condition at the production well. Figure 4(a) shows the comparison of gas production when BC1 (fixed well temperature) and BC2 (no heat conduction at production well) are applied for the laboratory case. Figure 4(b) shows the same comparison for the field case. In both cases, the temperature boundary condition does not significantly influence the gas production behavior. The difference between the gas production for the two different temperature boundary conditions in the field case is negligible, as indicated by the fact that the two gas production curves almost overlie each other. Figure 5(a) and (b) show the in situ temperature profiles for the laboratory case and the field case, respectively. Clearly, BC1 creates longitudinal heat conduction from the production well to the system, while BC2 does not. In both laboratory and field cases, the longitudinal heat conduction plays a small role in heat transfer in comparison with other terms including heat convection, surrounding heat conduction (transverse heat conduction) and latent heat of dissociation, but it does play a relatively more important role in the laboratory-scale in comparison with the field-scale, due to the relatively smaller size

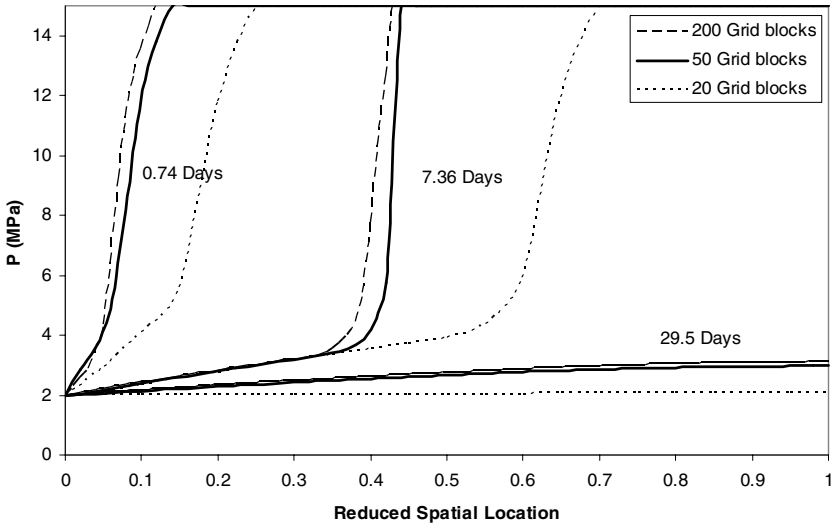

Figure 3. The pressure profiles of simulations with different number of grid blocks.

of the laboratory-scale medium. The temperature information of the production well is confined to a narrow region adjacent to the well in the field case. This observation seems to imply that "vertical" production well heating may not be very effective for inducing dissociation at the reservoir-scale.

To determine the sensitivity of the hydrate depressurization to thermal parameters in the field case, we changed the longitudinal heat conduction coefficient in the dissociated zone (λ_D in Figure 6), the longitudinal heat conduction coefficient in the untouched hydrate zone (λ_H in Figure 6) and transverse heat transfer coefficient (α) one at a time and compared the corresponding gas production behavior. Figure 6 shows the comparison. As can be seen from the figure, a decrease in the heat transfer coefficient causes a significant decrease of the gas production, while the effect of the longitudinal heat conduction coefficients, both in the dissociated zone and the untouched hydrate zone, is not so pronounced. The heat from surroundings comes directly to the dissociating zone because this model is 1-D; a 3-D model will show more sensitivity on heat conductivity. The heat transfer coefficient in the 1-D model is not independent of the heat conductivity in the hydrate zone; though they were varied independently in this comparison.

Figure 7 shows the front location evolution for the two (laboratory and field) base cases, i.e., non-isothermal simulation with BC1 as the temperature boundary condition at the well. The dissociation front location was defined as the right most location where the local pressure is below the equilibrium dissociation pressure (corresponding to the local temperature). The front location curves for the two cases have different shapes. The front location

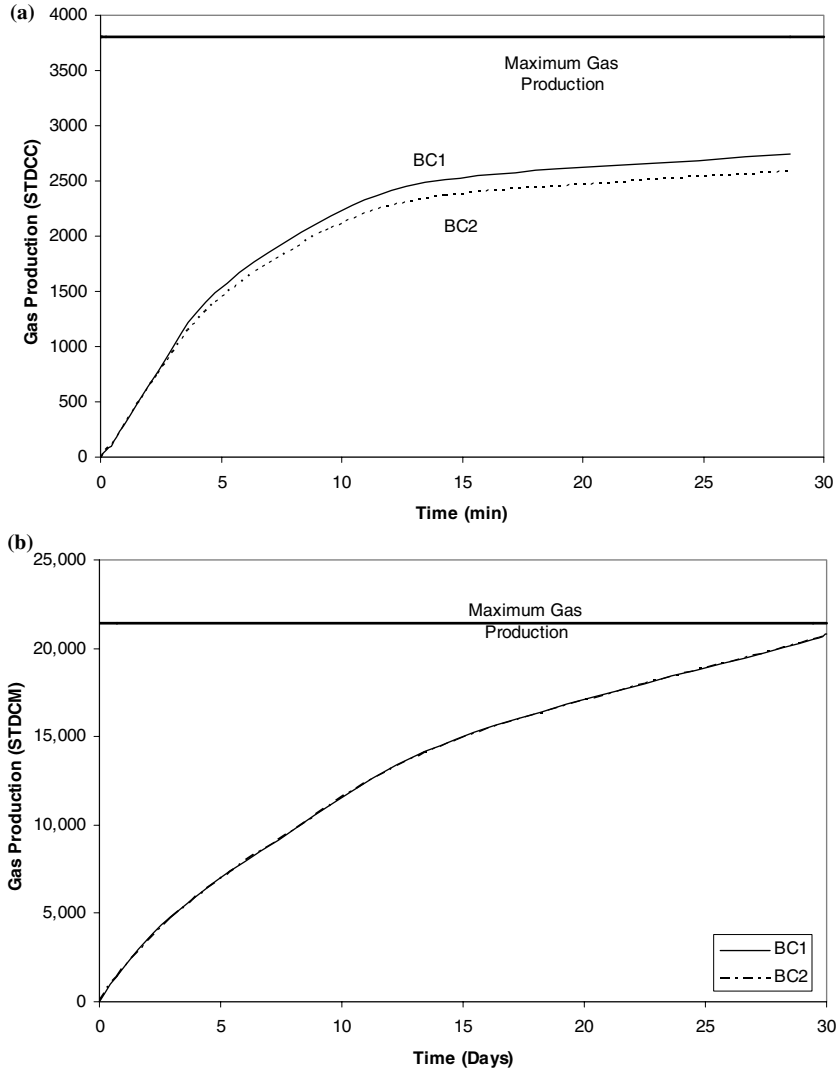

Figure 4. (a) Gas production comparison between BC1 and BC2 for laboratory-scale. (b) Gas production comparison between BC1 and BC2 for field-scale.

reaches the end of the medium immediately after the start of the depressurization in the laboratory-scale, while it evolves gradually in the field-scale. Self-similar solution assuming equilibrium dissociation (Ji *et al.*, 2001) predicts a front speed proportional to $\sqrt{t}$, which is different from that observed in the field-scale. Clearly, this prediction does not apply to the laboratory-scale considered here at all. After a sudden ejection of fluid from the medium, which corresponds to the jump occurring in the first stage in the curve for

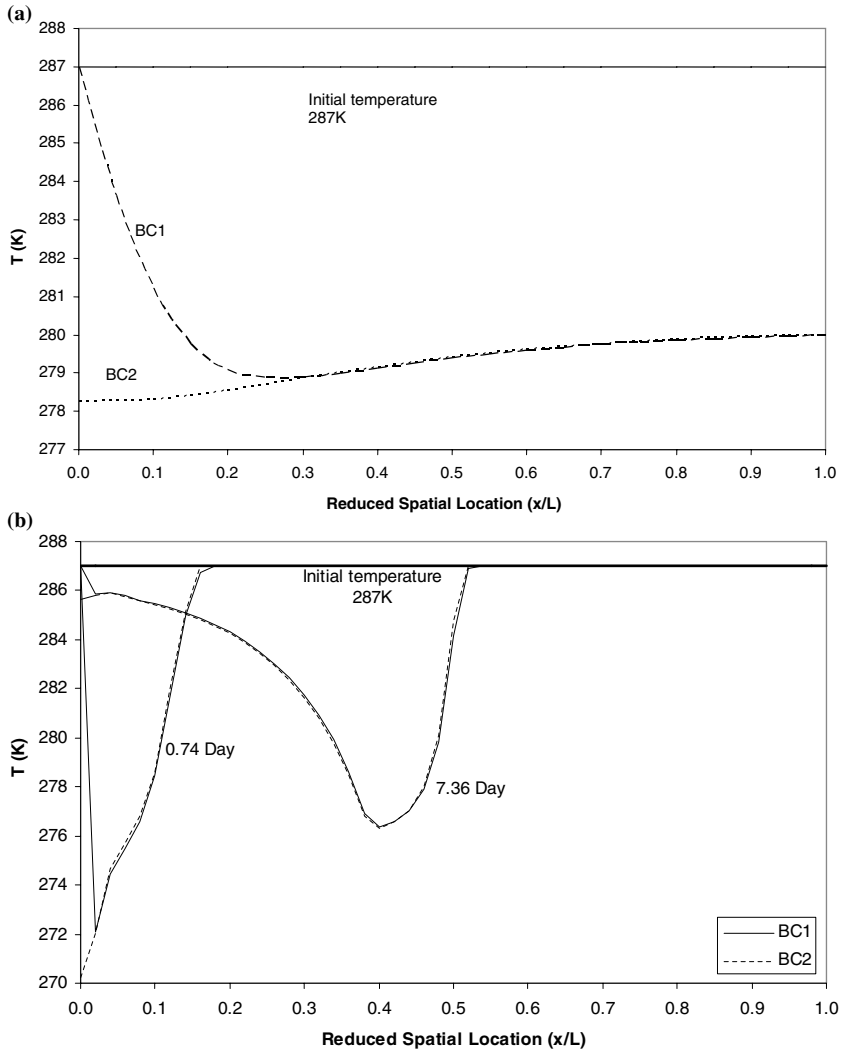

Figure 5. (a) Temperature distribution comparison between BC1 and BC2 for laboratory-scale at 4.77 min. (b) Temperature distribution comparison between BC1 and BC2 for field-scale.

laboratory-scale, the dissociation occurs almost uniformly through the hydrate-bearing medium. Decrease of the permeability expands the time range of the first stage. If the permeability is decreased a lot, a flow-limited regime would be obtained and the production curve would be similar to the one for the field example shown in Figure 7.

Figure 8 shows the comparison of the cumulative gas production for different dissociation constant, k_d. The corresponding values of R_τ are

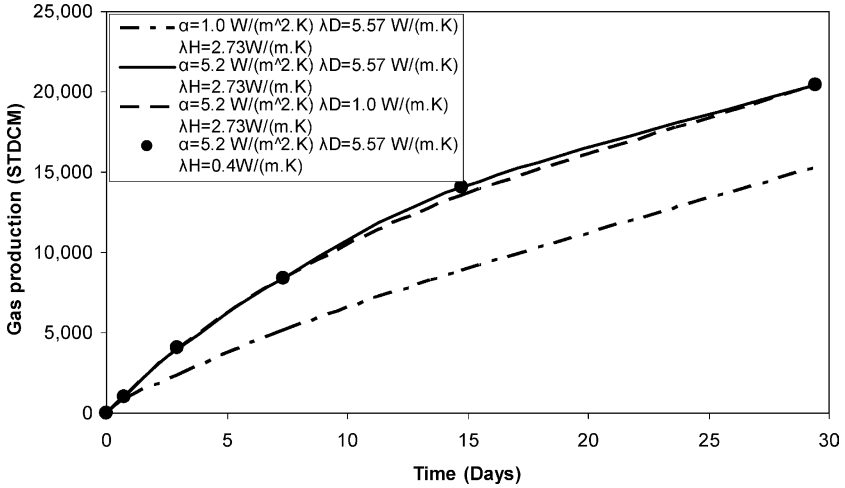

Figure 6. Effects of longitudinal heat conduction and transverse heat transfer on gas production (α is the transverse heat transfer coefficient; λ_D is the longitudinal heat conduction coefficient in the dissociated zone; λ_H is the longitudinal heat conduction coefficient in the untouched hydrate zone).

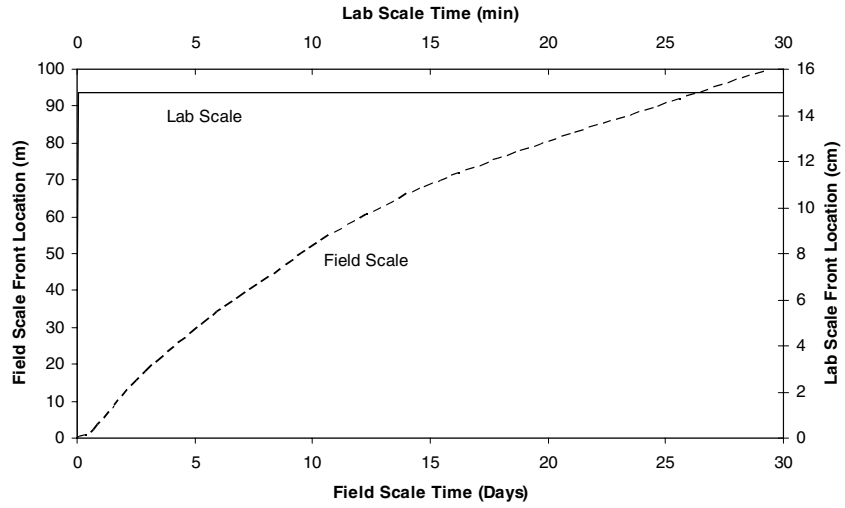

Figure 7. Front location evolution in field-scale and laboratory-scale.

specified next to the curves. As expected, for the field case, the production does not change significantly, as k_d goes up. The field-scale depressurization is flow-limited, as indicated by $R_\tau \ll 1$. This sensitivity is high for the laboratory-scale because it is dissociation-limited, as can be seen from Figure 8. In field cases, increasing k_d would not improve the efficiency of gas production from hydrate reservoir, if it is flow-limited.

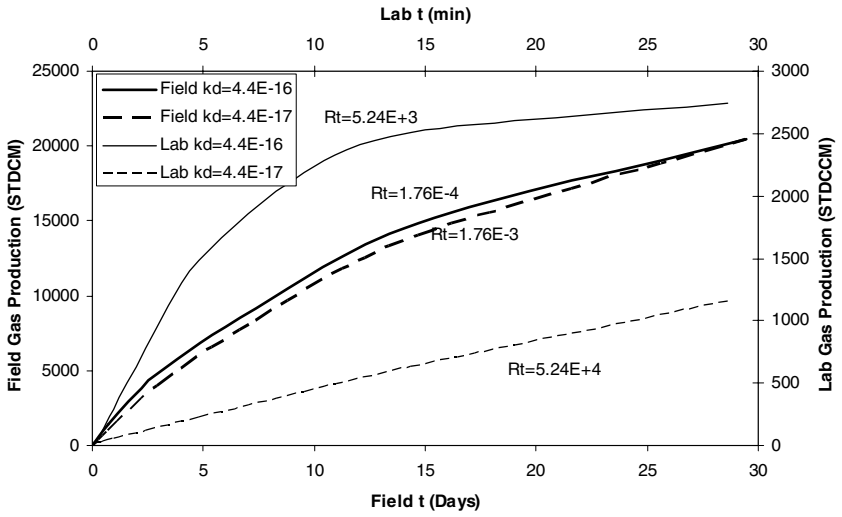

Figure 8. Gas production with different dissociation constants for both scales.

Yousif *et al.* (1991) conducted an experiment in laboratory to study the performance of hydrate dissociation through depressurization of a methane hydrate core sample, which had been artificially made with a Berea sandstone. In this work, we tried to match their experimental data of gas production and dissociation front location with the simulator. In the experiment, the core sample was put in a liquid bath with constant temperature of 273.7 K; so BC1 was used in this non-isothermal simulation. Figures 9 and 10 show the fitting curves for the gas production and front location, respectively. To match these curves, the following permeability was used:

$$K = \begin{cases} 5.51721 \times 10^{-3} (\phi_{\mathrm{wg}})^{0.86}, & \phi_{\mathrm{wg}} < 0.11, \\ 4.84653 \times 10^{5} (\phi_{\mathrm{wg}})^{9.13}, & \phi_{\mathrm{wg}} \geqslant 0.11. \end{cases} \tag{4.1}$$

The unit of the permeability calculated in Equation (4.1) is md. By comparing Equation (4.1) and Equation (2.10), we can see that the Equation (4.1) gives a permeability 1/1000 of that given by Equation (2.10). This low permeability perhaps is due to the blockage of the pore space by hydrate particles during the hydrate formation process or by the ice particles formed during the hydrate formation process or by the ice particles formed during the hydrate dissociation process, thus the effective porosity is significant lower than the actual porosity used to evaluate the absolute permeability. Simulation results show that the process is limited by dissociation. Also shown in Figures 9 and 10 are the curves obtained from isothermal simulation and BC2 with the same permeability and equilibrium dissociation

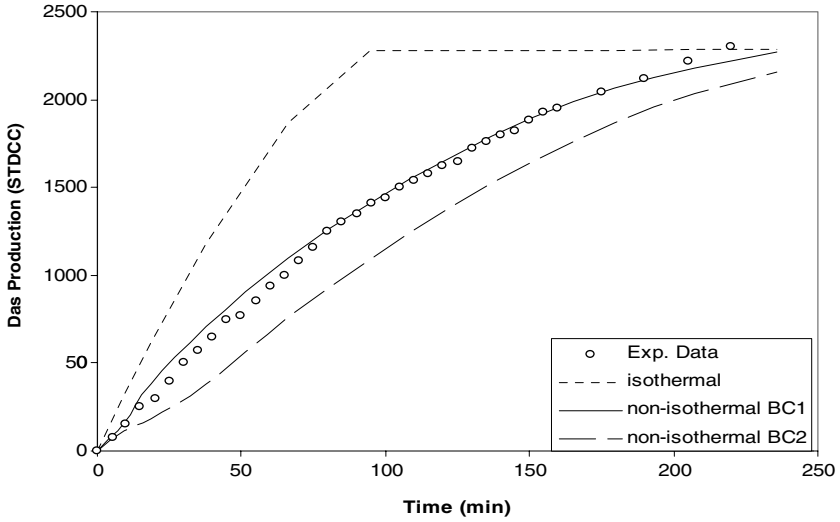

Figure 9. Fitting of the experimental data of gas production.

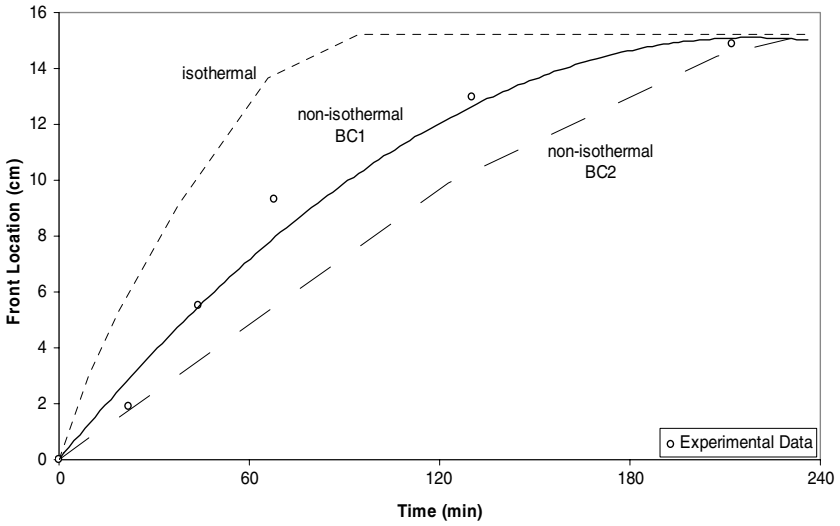

Figure 10. Fitting of the experimental data of front location.

pressure. Clearly, the isothermal simulation evolves the process faster than the non-isothermal because local temperature decrease is not modeled. BC2 simulation evolves more slowly than BC1 because heat conduction from the production well is neglected.

For hydrate deposits, where the water (connate plus the amount produced from hydrate) is immobile, Ji *et al*. (2001) proposed a self-similar

solution for the depressurization process. This solution is proposed to be applicable at low initial hydrate saturations. In order to compare the results of the numerical simulation with the analytical solution, a sample case was run with the initial conditions of $S_h^0 = 0.19, S_g^0 = 0.81$, and $S_w^0 = 0$. Note that the initial gas saturation is much higher and the water saturation is much lower than the base case. The other parameters have the same values as that used in the base case field-scale simulation. Figure 11 shows the comparison of the pressure field. The self-similar solution is for a semi-infinite system; we show the pressure for the first 100 m from the production well. The numerical solution shows a faster decrease in pressure than the self-similar solution. The analytical method assumes that k_{rg}, Z, T, S_g and μ_g are independent of position and time within the dissociated zone (and the hydrate zone) to derive a linearized pressure equation. These approximations are inconsistent with the results of the analytical solution itself, where Z, T, etc. vary within the dissociated zone. The pressure profile for the numerical solution is very different from that of the analytical solution, indicating that the approximations are inconsistent and unrealistic.

The self-similar solution gives a fixed dissociation temperature at 276 K for the reservoir under the given conditions. This corresponds to a dissociation pressure of about 4 MPa, which is much lower than the dissociation pressure obtained from the numerical simulation in this work. The numerical solution gives a dissociation temperature roughly between 282 and 285 K,

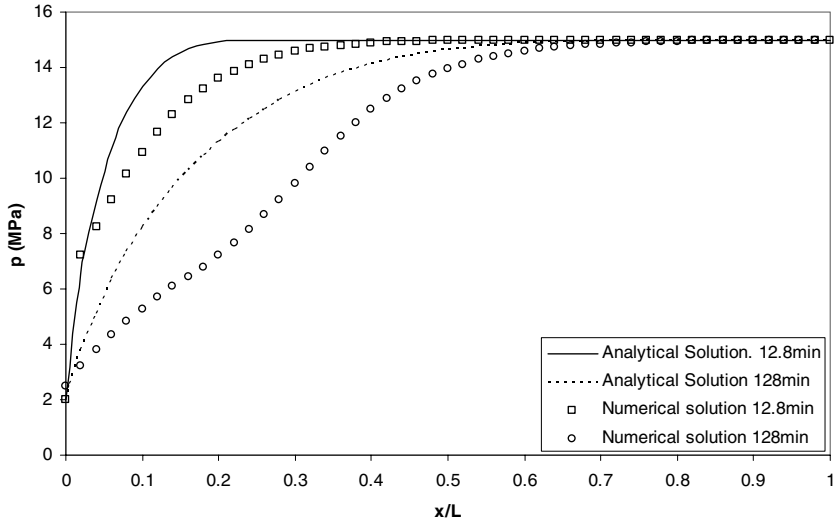

Figure 11. Pressure profile comparison between the numerical solution and the self-similar solution.

corresponding to a dissociation pressure between 7 and 10 MPa. In fact, numerical results show that the throttling effect, which is included in the self-similar solution model, affects the temperature field to an insignificant extent in the numerical model, except near the production well, where the pressure gradient is higher. The analytical solution neglects the dissociation enthalpy change and heat conduction from surroundings in prediction of the temperature distribution. These effects are very important for accurate simulation of depressurization.

6. Conclusions

Methane gas production from hydrate containing porous media by depressurization is studied. A non-isothermal one-dimensional simulator is developed. This model differs from previous analytical self-similar model by taking into account the complete heat balance equation, heat transfer from surroundings, kinetics associated to hydrate decomposition and flow of water as a result of hydrate dissociation. The following are the conclusions drawn from the results,

- The parameter, R_τ, proposed in this work determines whether the process is dissociation-limited or flow-limited. The field-scale processes are often flow-limited. The laboratory-scale process can be dissociation-limited if the permeability is high enough. The production rate does not change much with the kinetic rate if a process is flow-limited.
- Different temperature boundary conditions at the production well do not make a significant difference to the gas production rate at the field-scale. Heating the formation through vertical production wells is inefficient. Other modes of heating should be considered.
- Gas production rate from a linear reservoir is more sensitive to the heat transfer coefficient with the surrounding than the longitudinal heat conduction coefficient, in 1-D simulations.

Accurate simulation of hydrate depressurization requires accurate petrophysical and thermophysical data. Improvement in sampling and remote sensing of hydrate deposits is needed to better characterize existing fields. Laboratory study of both natural samples and artificial gas hydrates to determine petrophysical and thermophysical properties is difficult, but critically needed.

Acknowledgements

The authors gratefully acknowledge the support of the Westport Technology Center International and the US Department of Energy.

References

Amyx, J. W., Bass, D. M. and Whiting, R. L.: 1960, *Petroleum Reservoir Engineering-Physical Properties*, McGraw-Hill, New York.

Clarke, M. and Bishnoi, P. R.: 2000, Determination of the intrinsic rate of ethane gas hydrate decomposition, *Chem. Eng. Sci.* **55**, 4869–4883.

Clarke, M. and Bishnoi, P. R.: 2001, Determination of the active energy and intrinsic rate constant of methane gas hydrate decomposition, *Can. J. of Chem. Eng.* **79**(2), 143–147.

Ji, C., Ahmadi, G. and Smith, D. H.: 2001, Natural gas production from hydrate decomposition by depressurization, *Chem. Eng. Sci.* **56**, 5801–5814.

Kim, H. C., Bishnoi, P. R., Heidemann, R. A. and Rizvi, S. S. H.: 1987, Kinetics of methane hydrate dissociation, *Chem. Eng. Sci.* **42**(7), 1645–1653.

Kvenvolden, K. A., Carlson, P. R. and Threlkeld, C. N.: 1993, Possible connection between two Alaskan catastrophes occurring 25 years apart (1964 and 1989), *Geology* **21**, 813–816.

Makogan, Y. F.: 1997, Hydrates of hydrocarbons, PennWell Books, Tulsa, Oklahoma.

Makogon, Y. F. and Holditch, S. A.: 2001, Experiments illustrate hydrate morphology and kinetics, *Gas and Oil J.* 45–50.

Moniz, E. J. and Kenderdine, M. A.: 2002, Meeting energy challenges: technology and policy, *Physics Today* **55**, 40–46.

Moridis, G. J.: 2002, Numerical studies of gas production from methane hydrates, *SPE* 60693, *proc. SPE Gas Tech. Symposium*, Calgary, April 30–May 2.

Nozad, I., Carbonell, R. G. and Whitaker, S.: 1985, Heat conduction in multiphase systems. I. Theory and experiment for two-phase systems, *Chem. Eng. Sci.* **40**, 843–855.

Selim, M. S. and Sloan, E. D.: 1989, Heat and mass transfer during the dissociation of hydrate in porous media, *AIChE J.* **35**, 1049–1052.

Skov, A. M.: 2003, World energy beyond 2050, *J. of Petroleum Technol.* **55**(1), 34–37.

Sloan, E. D.: 1998, Clathrate hydrates of natural gases, 2nd ed., Marcel Dekker, New York.

Stern, L. A., Kirby, S. H. and Durham, W. B.: 1996, Peculiarities of methane clathrate hydrate formation and solid-state deformation, including possible superheating of water ice, *Science* **273**, 1843–1848.

Tester, J. W.: 1997, Thermodynamics and Its Applications, 3rd ed., Prentice Hall, New Jersey.

Tsypkin, G. G.: 1991, Effect of liquid phase mobility on gas hydrate dissociation in reservoirs, *J. of Fluid and Gas Mechanics* **4**, 105–114.

Wilder, J. W. and Smith, D. H.: 2002, Dependencies of clathrate hydrate dissociation fugacities on the inverse temperature and inverse pore radius, *Ind. Eng. Chem. Res.* **41**, 2819–2825.

Yousif, M. H., Abass, H. H., Selim, M. S. and Sloan, E. D.: 1991, Experimental and theoretical investigation of methane-gas-hydrate dissociation in porous media, *SPE Res. Eng.* **6**, 69–76.